

The Structure–Property Investigation of $\text{Bi}_{1-x}\text{Ce}_x\text{FeO}_3$ ($x = 0, 0.05$)–Li Battery: *In Situ* XRD and XANES Studies

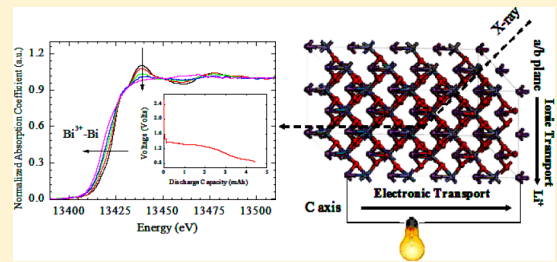
Xingmin Zhang,[†] Mei Gao,[‡] Yueliang Gu,[‡] Hongliang Bao,[†] Xiaolong Li,[‡] Xingtai Zhou,[†] and Wen Wen^{*,‡}

[†]Shanghai Institute of Applied Physics, Chinese Academy of Sciences, 2019 Jialuo Road, Shanghai 201800, P. R. China

[‡]Shanghai Synchrotron Radiation Facility, Shanghai Institute of Applied Physics, Chinese Academy of Sciences, 239 Zhangheng Road, Pudong New Area Shanghai 201204, P. R. China

Supporting Information

ABSTRACT: BiFeO_3 and $\text{Bi}_{0.95}\text{Ce}_{0.05}\text{FeO}_3$ were synthesized via a coprecipitation technique. During the synthesis process, the phase transitions were monitored via *in situ* synchrotron X-ray diffraction (XRD). The Ce addition increased the formation temperature of BiFeO_3 phase, while greatly suppressed the particle size growth. $\text{Ce}_{0.05}\text{Bi}_{0.95}\text{FeO}_3$ was further employed for lithium battery application, and good electrochemical cycling performance was observed between 1.15 and 3.0 V. Ce addition not only increased the discharge capacity but also displayed 0.15 V higher discharge voltage (in the second cycle), compared with BiFeO_3 . After 2 Li ions insertion, Bi ions are reduced to metallic Bi and separated out of the perovskite lattice. In the following charge process, metallic Bi can be oxidized back to its ionic state. Elevated discharge voltage was observed in the second discharge process. a/b -axis lattice parameters are mainly changed by Li intercalation/deintercalation, and c -axis lattice parameters are heavily affected by the ionic species in the c -axis. There are two distinct conduction pathways: one is the ionic conduction along the a/b -plane, and the other is the electronic conduction along the c -axis.



1. INTRODUCTION

In a lithium ion battery, Li^+ ions are usually shuttled in/out of the host lattice, with concomitant reduction/oxidation of certain elements to balance the charge. Thus, usually there are elements with variable oxidation states in the host matrix. This is so-called the redox couple, which is usually cationic, such as $\text{Co}^{3+}/\text{Co}^{4+}$ (in LiCoO_2),^{1,2} and could also be anionic, such as $\text{O}^{2-}/\text{O}^{-1-4}$. The latter was observed in systems such as LiNiO_2 ,³ LiCoO_2 ,^{1,2} and lithiated LiMn_2O_4 ,⁴ etc. Recent studies of the transition metal based oxides/fluorides also shed light on another mechanism for discharge, where the host matrix decomposed to metallic nanoclusters embedded in $\text{Li}_2\text{O}/\text{LiF}$, and the reversible system is consisted of metal/metal oxide (metal fluoride) during the Li^+ shuttling process.⁵⁻⁹ The decomposition of host into metallic state often involves a larger number of electron transfers compared with other systems such as LiFePO_4 , LiCoO_2 , and LiMn_2O_4 , and thus, larger discharge capacities are obtained.

Perovskite ABO_3 is a ternary transition metal oxide and is of great interest in applications such as fast ionic conductor,¹⁰ solid electrolyte,¹¹ and superconductor¹² due to their excellent O^{2-} mobility. Some perovskite oxides even have combined ionic and electronic conductivity, which potentially enable very good transportation pathways for both lithium ions and electrons.¹³⁻¹⁵ In the literature, some perovskite oxides have been used for lithium battery applications, such as SrSnO_3 ,¹⁶ BiFeO_3 ,^{17,18} LaFeO_3 ,¹⁹ CaSnO_3 ,²⁰ $\text{Gd}_{1/3}\text{TaO}_3$,²¹

$\text{Li}_y\text{La}_{(1-y)/3}\text{NbO}_3$,²² SrVO_3 ,²³ and LaCoO_3 ,²⁴ etc. However, detailed structure–property investigations are not explored in detail and limit the understanding to their discharge mechanism. As the consequence, it is hard to find the future directions to further enhance their performance.

BiFeO_3 is one of few perovskite oxides (the other is SrSnO_3) that display a discharge capacity more than 1000 mAh/g.¹⁶⁻¹⁸ During the discharge, metallic Bi was separated out from the crystal lattice and LiBi alloy formation was observed. Further *in situ* X-ray absorption near-edge structure (XANES) spectra revealed that Bi ions are mainly responsible for charge transfer during the electrochemical cycling process, while Fe ions are mainly used to stabilize the BiFeO_3 lattice. This is different from the discharge mechanisms of the other reported perovskites, such as SrSnO_3 ,¹⁶ LaCoO_3 ,²⁴ $(\text{Li},\text{La})\text{TiO}_3$,²⁵ and $\text{Gd}_{1/3}\text{TaO}_3$,²¹ etc., where the transition metals at B sites (Sn, Co, Ti, and Ta) are responsible for the charge transfer. It is also different from the discharge mechanism of BFeO_3 ,²⁶ (please note that B and Bi belong to the same main group) where the Fe ions are mainly responsible for charge transfer. At this stage, these differences that might be very important to future directions are not well-clarified.

Received: July 3, 2012

Revised: August 28, 2012

Published: August 28, 2012



In this paper, we synthesized $\text{Bi}_{1-x}\text{Ce}_x\text{FeO}_3$ ($x = 0, 0.05$) using a coprecipitation technique. Further, the electrochemical performance is evaluated, and the detailed discharge mechanism was investigated using combined *in situ* XRD and XANES techniques. The structure and property relationship of $\text{Bi}_{0.95}\text{Ce}_{0.05}\text{FeO}_3$ -Li battery was successfully correlated.

2. MATERIALS SYNTHESIS AND CHARACTERIZATION

2.1. Materials Synthesis. $\text{Bi}_{0.95}\text{Ce}_{0.05}\text{FeO}_3$ was synthesized using a coprecipitation technique. During the synthesis, stoichiometric amounts of $\text{Fe}(\text{NO}_3)_3 \cdot 9\text{H}_2\text{O}$, $\text{Bi}(\text{NO}_3)_3 \cdot 6\text{H}_2\text{O}$, and $\text{Ce}(\text{NO}_3)_3 \cdot 5\text{H}_2\text{O}$ were dissolved in distilled water and were stirred until all the solids were dissolved. A small amount of dilute nitric acid was added to fully dissolve the solids. Then $\text{NH}_3 \cdot \text{H}_2\text{O}$ was dropwise added into the solution and precipitated the Ce, Fe, and Bi ions. $\text{NH}_3 \cdot \text{H}_2\text{O}$ was added until there were no obvious precipitates appeared after further addition, and the pH of the solution was adjusted to about 10. The solution was dried at $\sim 80^\circ\text{C}$ and then transferred to a muffing furnace at $\sim 250^\circ\text{C}$ to remove the NO_3 group for ~ 6 h. The solid sample was collected and ground into a fine powder. The precursor was heated in a muffing furnace at various temperatures for 3 h. After experiments, the furnace was cooled down naturally to ambient temperature. The samples were stored for future experiments. The synthesis of BiFeO_3 exactly followed the same route, except that there was no $\text{Ce}(\text{NO}_3)_3 \cdot 5\text{H}_2\text{O}$ in the starting materials.

2.2. In Situ XRD during Heating Process. The *in situ* XRD during the heating process were performed at BL14B1 of the Shanghai Synchrotron Radiation Facility at a wavelength of 1.2398 Å. BL14B1 is a bending magnet beamline, and the storage ring energy of SSRF is 3.5 GeV. The beam is first collimated using a Rh/Si mirror and then is monochromatized using a Si(111) double crystal monochromator.¹⁷ After that, the beam is further focused by a Rh/Si mirror to the size of 0.5 mm \times 0.5 mm. Higher order harmonics are also rejected by the Rh/Si mirror to 3×10^{-4} . A Mar345 image plate detector was employed for data collection, and the data were further integrated using a fit2d code. A typical amount of precursor (1–2 mg) was inserted into a flow cell^{27–29} (quartz capillary tube with diameter of ~ 1 mm), and some glass wool was placed at both sides of the sample to prevent it from moving. Heating wire (resistance heater, $\text{Ni}_{80}\text{Cr}_{20}$ alloy with a diameter of 0.5 mm) was wrapped outside of the quartz tube, and a thermocouple (diameter of 0.6 mm) was placed close to the sample for accurate temperature measurements. The XRD data were further analyzed using CMPR for scaling,³⁰ data subtraction, peak fitting, and related analysis. The *ex situ* XRD patterns were obtained at Beamline BL14B1 using a NaI point detector with a step size of 0.02 degrees.

2.3. Scanning Electron Microscopy. The scanning electron microscopy measurements were carried out on a LEO 1530VP.

2.4. Galvanostatic Cycling. The electrochemical galvanostatic cycling was carried out at a current density of ~ 20 mA/g. Typically, $\text{BiFeO}_3/\text{Bi}_{0.95}\text{Ce}_{0.05}\text{FeO}_3$, PVDF (poly(vinylidene fluoride)), and acetylene black were mixed in the weight percentage of 75%, 12.5%, and 12.5% in NMP (*N*-methyl-2-pyrrolidone) and then coated on a 0.01 mm Cu foil to make the electrode. The NMP is evaporated by drying in a vacuum oven for 4 h at 120°C . The counter electrode is a piece of metallic lithium. Cu foils were used as the current collectors for both the anode and cathode sides.

2.5. In Situ XRD during the Electrochemical Cycling.

The *in situ* X-ray diffraction (XRD) experiments during the electrochemical cycling process were carried out at BL14B1 beamline of the Shanghai Synchrotron Radiation Facility (SSRF) at a wavelength of 1.2398 Å. An image plate detector was used for data collection, and a fit2d code is employed to integrate the diffraction ring. LaB_6 was used for calibration. The XRD data were analyzed using the CMPR program for peak fitting, scaling, etc.³⁰ The *in situ* experiments were carried out using a spectroelectrochemical cell,^{31,32} which has been discussed in detail elsewhere. It is a sandwich-type cell feature, which has Mylar windows in both the cathodic and anodic sides. This allows the X-rays to penetrate through the active material while it is cycled. The *in situ* cell is airtight, and thus any structural transformations observed are not because of decomposition or oxidation of the material upon air exposure. For *in situ* work, the middle of the Cu current collectors was cut a hole (2 mm \times 2 mm) for better beam path. For *in situ* XRD work, the painted electrode materials were peeled off from the Cu foil in order for better signal.

2.6. In Situ Bi-L_{III} Edge X-ray Absorption Spectroscopy.

The Bi-L_{III} edge *in situ* X-ray absorption experiments were carried out at BL14W1, which is a wiggler-based beamline, of the Shanghai Synchrotron Radiation Facility (SSRF) using a transmission mode.^{33,34} An Si(111) double crystal monochromator cooled by liquid N_2 was employed to monochromatize the energy. The gases used for I_0 and I_t chambers are N_2 and Ar, respectively. The XANES data were analyzed by Athena code of the IFEFFIT program for background removal, E_0 selection, normalization, etc.³⁵ An *in situ* spectroelectrochemical cell was employed for *in situ* characterizations similar to those used for *in situ* XRD experiments. The middle of the Cu current collectors was cut a hole (2 mm \times 2 mm) for better beam path.

2.7. XRD Data Profile Fitting. The XRD data were fitted using the EXPGUI code, using the combination of a Lorenzian and Gaussian profiles.^{36–38} The atomic positions of BiFeO_3 was referred to Reyes et al.³⁹

3. RESULTS AND DISCUSSION

3.1. In Situ XRD Pattern during Heating. The *in situ* X-ray diffraction patterns collected during the heating process of BiFeO_3 are displayed in Figure 1a. The starting material is amorphous. The XRD patterns displayed in Figure 1 are the difference spectra (subtract the diffraction pattern of the first one) and are very sensitive to phase transitions. Around 269.4°C , the diffraction peaks of $\text{Bi}_{24}\text{Fe}_{39}$ ⁴⁰ appeared, and it changed to $\text{Bi}_{25}\text{Fe}_{40}$ ⁴¹ at 389.4°C . The obvious difference between these two is that for $\text{Bi}_{25}\text{Fe}_{40}$ there is a diffraction peak located at 2theta of 24.5 (222). The BiFeO_3 phase appeared around 400°C . The diffraction peaks of BiFeO_3 increased gradually with the increase of temperature, while the diffraction peaks of $\text{Bi}_{25}\text{Fe}_{40}$ decreased concomitantly.

The *in situ* X-ray diffraction patterns collected during the heating process of $\text{Bi}_{0.95}\text{Ce}_{0.05}\text{FeO}_3$ were displayed in Figure 1b. Compared with those of BiFeO_3 , $\text{Bi}_{24}\text{Fe}_{39}$ phase appeared starting from 385.7°C , which is about 100°C higher compared with that in the heating of BiFeO_3 . Around 461.1°C , $\text{Bi}_{24}\text{Fe}_{39}$ transformed to the $\text{Bi}_{25}\text{Fe}_{40}$ phase. Similarly, the $\text{Bi}_{0.95}\text{Ce}_{0.05}\text{FeO}_3$ phase did not appear until 497.1°C , which is 97.1°C higher than the transition temperature observed for pure BiFeO_3 . The addition of 5% Ce into the precursor increased the synthesis temperature.

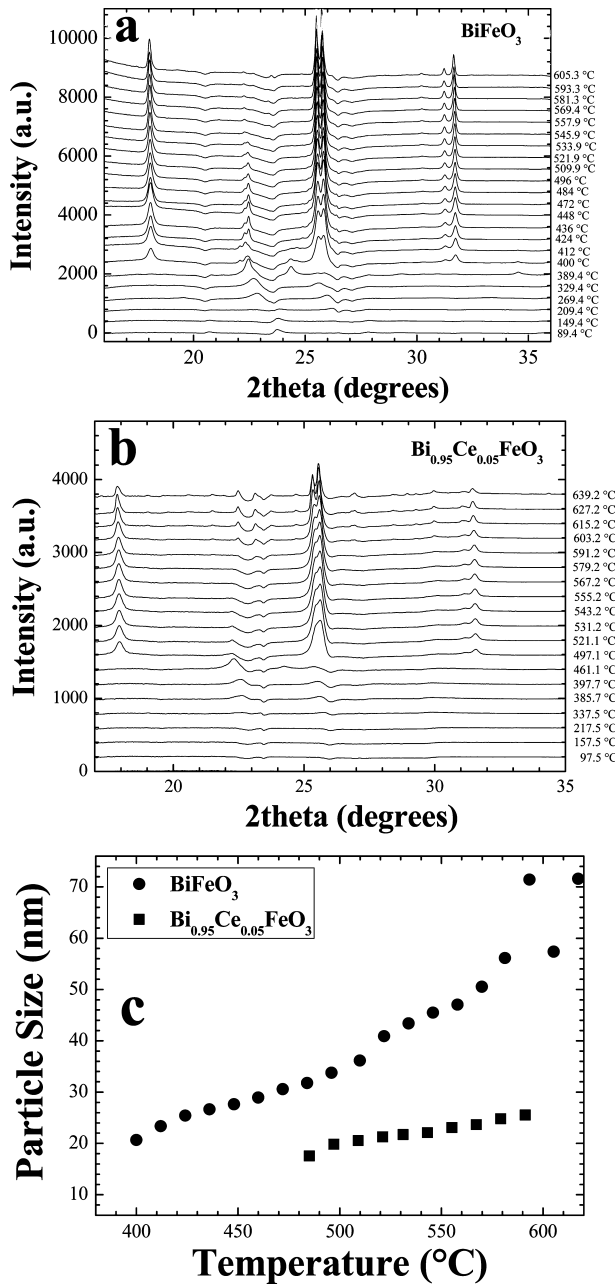


Figure 1. (a) The *in situ* differential XRD patterns collected during the synthesis of BiFeO_3 . The XRD patterns displayed have subtracted the diffraction pattern of the first one. (b) The *in situ* differential XRD patterns collected during the synthesis of $\text{Bi}_{0.95}\text{Ce}_{0.05}\text{FeO}_3$. The XRD patterns displayed have subtracted the diffraction pattern of the first one. (c) The change of particle size calculated from Scherer's equation. The *in situ* XRD data were taken at BL14B1 of SSRF at a wavelength of 1.2398 Å.

Using the CMPR program, the FWHM of the diffraction peaks was obtained by curve fitting. The average particle size was calculated according to Scherer's equation and is plotted in Figure 1c. The particle size of $\text{Bi}_{0.95}\text{Ce}_{0.05}\text{FeO}_3$ increased much slower compared with that of pure BiFeO_3 . The particle size of BiFeO_3 increased from ~20 nm at 400 °C to ~70 nm at 600 °C, while the particle size of $\text{Bi}_{0.95}\text{Ce}_{0.05}\text{FeO}_3$ increased from ~17 nm at 400 °C to ~25 nm at 600 °C. Obviously, the addition of 5% Ce greatly decreased the growth of the crystals.

3.2. Ex Situ Characterization of Synthesized Samples.

BiFeO_3 and $\text{Bi}_{0.95}\text{Ce}_{0.05}\text{FeO}_3$ were synthesized at various temperatures using the muffing furnace. The XRD patterns of the synthesized BiFeO_3 and $\text{Bi}_{0.95}\text{Ce}_{0.05}\text{FeO}_3$ are displayed in Figures 2a and 2b, respectively. For BiFeO_3 , the pure phase is obtained at 590 °C, and there are impurities observed at other temperatures. Most of the impurities are observed at 450 °C, where the major impurities can be indexed as the combination

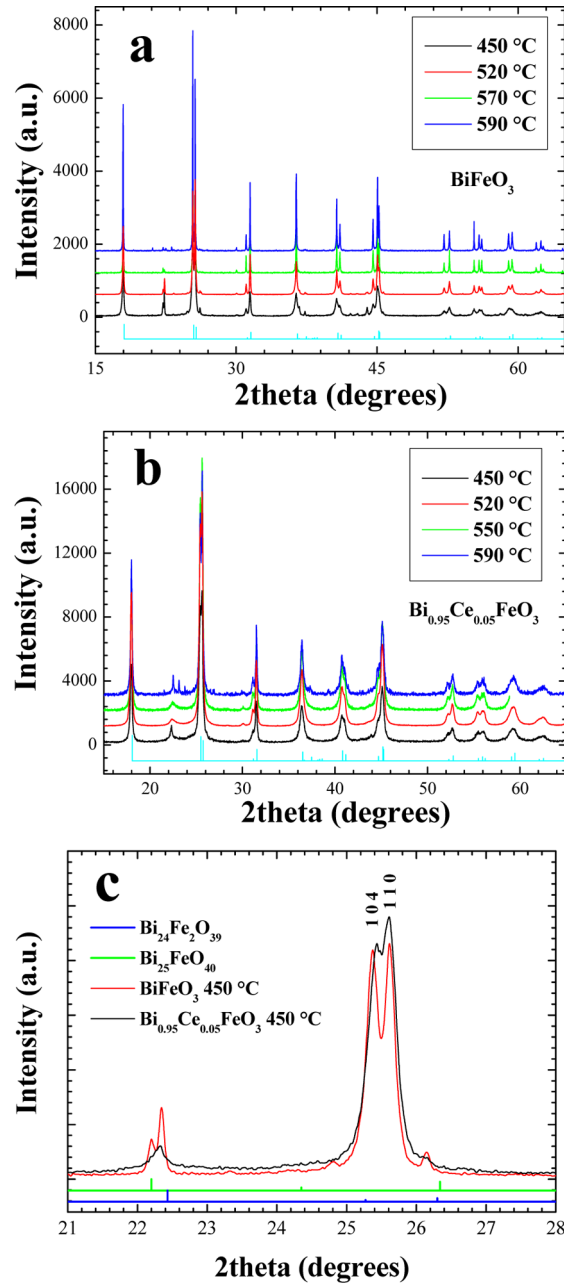


Figure 2. (a) XRD patterns of BiFeO_3 synthesized at 450 (black), 520 (red), 570 (green), and 590 °C (blue). The diffraction pattern of standard BiFeO_3 was displayed at the bottom (light blue). (b) XRD patterns of $\text{Bi}_{0.95}\text{Ce}_{0.05}\text{FeO}_3$ synthesized at 450 (black), 520 (red), 550 (green), and 590 °C (blue). The diffraction pattern of standard BiFeO_3 is displayed at the bottom (light blue). (c) Detailed view of diffraction patterns of BiFeO_3 (red) and $\text{Bi}_{0.95}\text{Ce}_{0.05}\text{FeO}_3$ (black) synthesized at 450 °C. The diffraction patterns of standard $\text{Bi}_{24}\text{Fe}_2\text{O}_{39}$ (blue) and $\text{Bi}_{25}\text{FeO}_{40}$ (green) are displayed at the bottom.

of $\text{Bi}_{24}\text{Fe}_2\text{O}_{39}$ and $\text{Bi}_{25}\text{FeO}_{40}$. There might have been a very small amount of $\text{Bi}_2\text{Fe}_4\text{O}_9$ ⁴² as well. As temperature increased, the impurities gradually transformed to BiFeO_3 phase. It is also observed that the X-ray diffraction peaks are much sharper as the increase of temperature. This is consistent with the *in situ* XRD studies and indicates the fast growth rate of the BiFeO_3 particles. For $\text{Bi}_{0.95}\text{Ce}_{0.05}\text{FeO}_3$, the purest phase was obtained at 520 °C. Compared with diffraction patterns of BiFeO_3 , those of $\text{Bi}_{0.95}\text{Ce}_{0.05}\text{FeO}_3$ are much broader (Figure 2c). This indicates that Ce doping greatly suppressed the particle size growth. It is also observed that (104) and (110) diffraction peaks of BiFeO_3 are much more resolved compared with those of $\text{Bi}_{0.95}\text{Ce}_{0.05}\text{FeO}_3$, which has also been observed in Ce-doped BiFeO_3 thin films.^{43,44} This indicated that Ce ions were successfully doped inside BiFeO_3 lattice.

The SEM images of the synthesized BiFeO_3 (520 °C) and $\text{Bi}_{0.95}\text{Ce}_{0.05}\text{FeO}_3$ (550 °C) are displayed in Figures 3a and 3b,

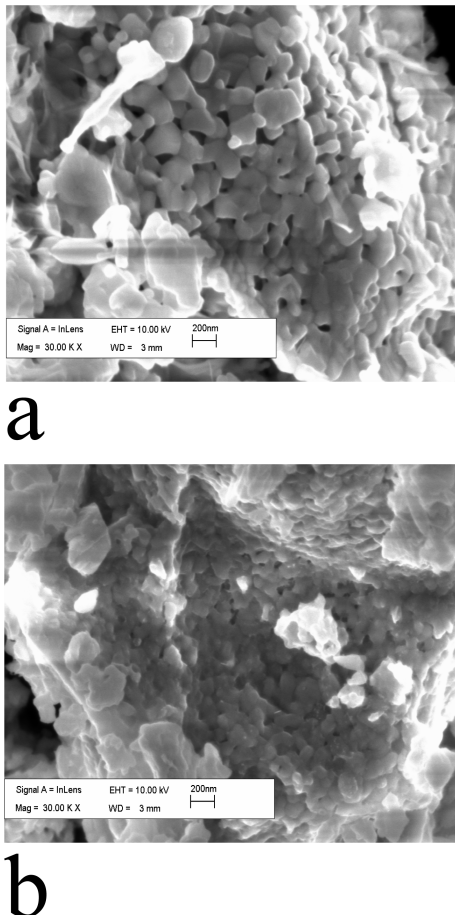


Figure 3. SEM images of (a) BiFeO_3 synthesized at 520 °C and (b) $\text{Bi}_{0.95}\text{Ce}_{0.05}\text{FeO}_3$ synthesized at 550 °C.

respectively. The typical particle size of BiFeO_3 is 200 nm × 150 nm, while they are not uniform. For $\text{Bi}_{0.95}\text{Ce}_{0.05}\text{FeO}_3$, the typical particles are ~40 nm × 50 nm, much smaller compared with those of BiFeO_3 . This is consistent with the XRD analysis.

The XRD patterns of BiFeO_3 and $\text{Bi}_{0.95}\text{Ce}_{0.05}\text{FeO}_3$ synthesized at different temperatures were fitted using the EXPGUI code. The typical fitting pattern is displayed in Figure 4. The diffraction peak (located at 2theta 22°) from the impurity phases of $\text{Bi}_{24}\text{Fe}_2\text{O}_{39}$ / $\text{Bi}_{25}\text{FeO}_{40}$ was excluded for much accurate refinement.

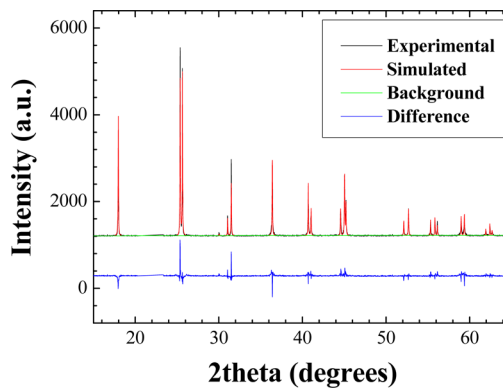


Figure 4. Typical fitting results using the EXPGUI code: black, experimental data; red, simulated; green, background; blue, difference of the experimental and simulated data. The sample is BiFeO_3 synthesized at 590 °C.

The lattice parameters of the synthesized samples are displayed in Table 1 for comparison. During the synthesis of

Table 1. Lattice Parameters (in Å) of $\text{Bi}_{1-x}\text{Ce}_x\text{FeO}_3$ ($x = 0$, 0.05, and 0.1) Synthesized at Various Temperatures (in °C)

temp	Ce amount		
	0%	5%	10%
450	<i>a</i>	5.5885	5.5875
	<i>c</i>	13.8910	13.8646
520	<i>a</i>	5.5864	5.5862
	<i>c</i>	13.8898	13.8598
550	<i>a</i>	5.5855	
	<i>c</i>	13.8588	
570	<i>a</i>	5.5865	
	<i>c</i>	13.8924	
590	<i>a</i>	5.5869	5.5848
	<i>c</i>	13.8920	13.8641

BiFeO_3 , the *a*-axis varies from 5.586 to 5.589 and the *c*-axis varies from 13.890 to 13.892 Å and are very similar. In $\text{Bi}_{0.95}\text{Ce}_{0.05}\text{FeO}_3$, the *a*-axis slightly decreased compared with BiFeO_3 synthesized at the same temperature (the largest difference is 0.002 Å at 590 °C), and the *c*-axis displayed a much larger decrease (the largest decrease is 0.03 Å at 520 °C). When the Ce amount increased to 10%, both *a*- and *c*-axis lattice parameters are further decreased. This indicates that Ce is effectively doped inside the lattice of BiFeO_3 , due to the smaller ionic radius of Ce^{3+} (1.03 Å) compared with that of the Bi^{3+} (1.08 Å). As discussed later, Bi tends to separate out of the crystal lattice in heavily lithiated BiFeO_3 and contributes to a large decrease of the *c*-axis lattice. The effect of Bi separation essentially has similar effects to the crystal lattice compared with the replacement of Bi^{3+} by Ce^{3+} .

3.3. Galvanostatic Cycling of BiFeO_3 –Li Battery. Figure 5a is the discharge profiles of a BiFeO_3 –Li battery with a cutoff voltage of 0.7 V. In the first discharge, there are two discharge plateaus and are located at 1.3 and 0.9 V, respectively. These are similar to the discharge behavior of BiFeO_3 reported earlier.^{17,18} In the following discharge cycles, higher discharge voltage are obtained due to structural transformations occurred during the first discharge process (Bi separation out of the ceramic lattice). The other features are similar to those reported earlier,¹⁷ except that much better capacity retention

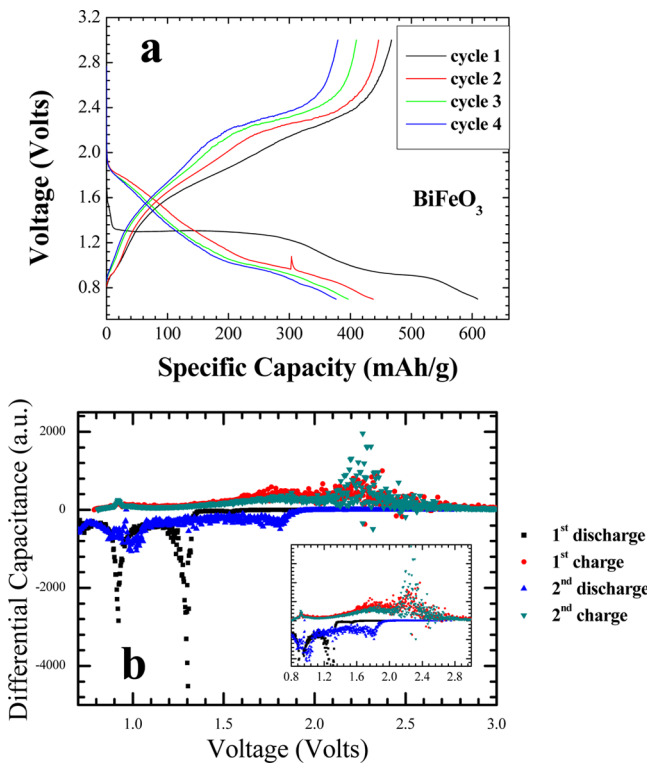


Figure 5. (a) Galvanostatic cycling profiles of BiFeO_3 -Li batteries with the voltage window between 0.7 and 3.0 V: black, cycle 1; red, cycle 2; green, cycle 3; blue, cycle 4. (b) Differential capacitance vs voltage plot of BiFeO_3 -Li battery using a cutoff voltage of 0.7–3.0 V: black, first discharge; red, first charge; blue, second discharge; dark green, second charge. Inset displays enlarged view. The BiFeO_3 used was synthesized at 590 °C for 3 h.

can be achieved, compared with BiFeO_3 synthesized by a molten salt techniques. The capacities of the following three discharge cycles are 450, 400, and 380 mAh/g compared to 400, 380, and 280 mAh/g reported before. This probably due to the smaller particle size of BiFeO_3 synthesized using the coprecipitation technique (200 nm × 150 nm), compared with that synthesized by the molten salt technique (300 nm).⁴⁵

The differential capacitance vs voltage plot of BiFeO_3 -Li battery (discharged between 0.7 and 3.0 V) is displayed in Figure 5b. In the first discharge cycle, two discharge peaks can be observed at 1.3 and 0.9 V. The first peak at 1.3 V corresponds to the reduction of Bi^{3+} to Bi^0 , and the second one at 0.9 V is related to lithium insertion into acetylene black.²² (LiBi alloy formation might also contribute to the 0.9 V peak).⁴⁶ In the first charge process, there are three peaks appeared at 0.9, 1.8, and 2.2 V. The latter two peaks are quite broad as well. For the peak at 0.9 V, it was assigned to the delithiation process from the acetylene black, since it displays similar intensity at both the first and second charge process. The broad peak located at 1.8 V was assigned to the dealloy process of LiBi. The third broad peak was assigned to the reoxidation of the metallic Bi to its ionic state, which latter was proved by *in situ* XANES. In the second discharge process, there is a broad peak appearing around 1.85 V followed by the second peak at ~1.0 V. After Bi separation from the ceramic matrix, the discharge voltage in the following discharge cycles is increased. The discharge peak at 1.85 V is about 0.35 V lower compared with that in the charge process (2.2 V) and was assigned to the reduction of ionic Bi ions to their metallic state.

For the discharge peak located ~1.0 V, its intensity increased in the second cycle and indicates that there is more LiBi formation. There is also a small peak located at 0.9 V, which was assigned to the lithium insertion into the acetylene black, similar to that observed in the first discharge process.

3.4. Galvanostatic Cycling of $\text{Bi}_{0.95}\text{Ce}_{0.05}\text{FeO}_3$ -Li

Battery. Further, the electrochemical cycling performance of $\text{Bi}_{0.95}\text{Ce}_{0.05}\text{FeO}_3$ -Li battery was studied using a cutoff voltage of 1.15 V (Figure 6a). The discharge profiles are very similar as those reported for transition metallic oxide as well as FeBO_3 ,^{5,6,26,34} where the batteries at first discharge at relatively

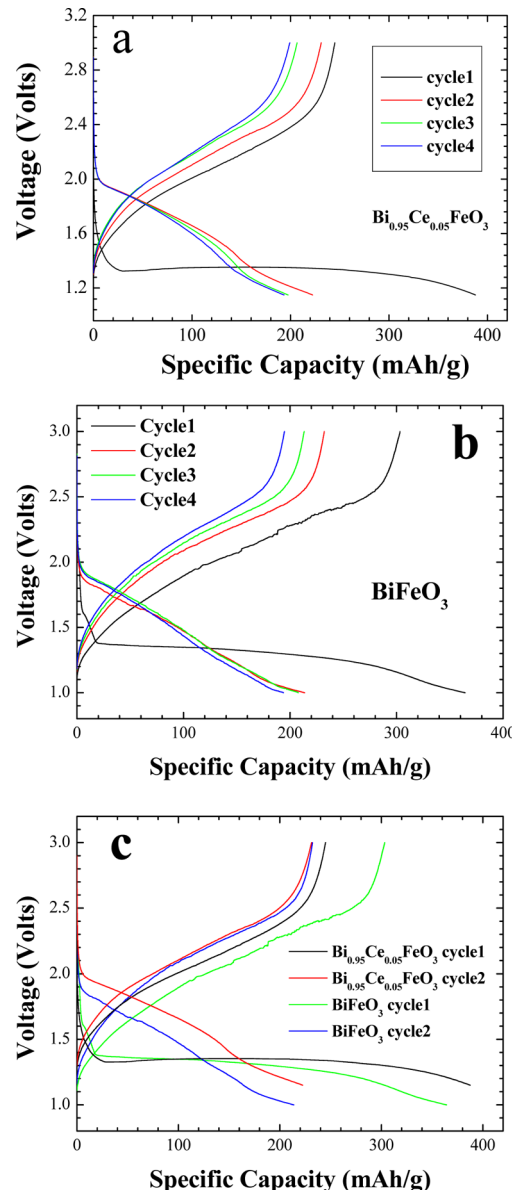


Figure 6. (a) Galvanostatic cycling profiles of $\text{Bi}_{0.95}\text{Ce}_{0.05}\text{FeO}_3$ -Li battery with the voltage window between 1.15 and 3.0 V: black, cycle 1; red, cycle 2; green, cycle 3; blue, cycle 4. (b) Galvanostatic cycling profiles of BiFeO_3 -Li battery with the voltage window between 1.0 and 3.0 V: black, cycle 1; red, cycle 2; green, cycle 3; blue, cycle 4. (c) Comparison of these two cycling profiles: black, cycle 1 of $\text{Bi}_{0.95}\text{Ce}_{0.05}\text{FeO}_3$ -Li battery; red, cycle 2 of $\text{Bi}_{0.95}\text{Ce}_{0.05}\text{FeO}_3$ -Li battery; green, cycle 1 of BiFeO_3 -Li battery; blue, cycle 2 of BiFeO_3 -Li battery. BiFeO_3 was synthesized at 590 °C for 3 h, and $\text{Bi}_{0.95}\text{Ce}_{0.05}\text{FeO}_3$ was synthesized at 520 °C for 3 h.

lower voltages with large capacity followed by elevated voltage discharges. The voltage drops quickly to about 1.35 V and reaches the first discharge plateau with a capacity about 400 mAh/g. In the first charge cycle, the voltage increases slowly to 3.0 V with a capacity about 250 mAh/g. The charge plateau is located between 1.8 and 2.3 V, which is much higher compared to the first discharge plateau. The discharge voltage of the second cycle is much higher compared with that of the first one, and a discharge capacity of ~230 mAh/g was achieved. As observed by *in situ* diffraction studies in the later section, this essentially indicates that Bi separates out of the perovskite lattice and increases the discharge voltage in the following electrochemical cycling. After first cycle, the electrochemical cycling profiles are similar, and the discharge capacity of ~200 mAh/g can still be obtained at the fourth discharge cycle.

For pure BiFeO_3 (Figure 6b), it displays a discharge voltage of ~1.35 V in the first discharge process, which is similar compared with that of $\text{Bi}_{0.95}\text{Ce}_{0.05}\text{FeO}_3$ (Figure 6c). However, in the following discharge cycles, the discharge voltage of BiFeO_3 -Li battery is about 0.15 V lower compared with that of $\text{Bi}_{0.95}\text{Ce}_{0.05}\text{FeO}_3$. This is the result of much smaller particle size of $\text{Bi}_{0.95}\text{Ce}_{0.05}\text{FeO}_3$, compared with that of BiFeO_3 , which enables much better electrochemical contact between the neighboring particles during the electrochemical cycling process. Also, the Ce doping might also increase the conductivity of the ceramic matrix and promote the charge transfer. It is also much easier to assemble batteries using $\text{Bi}_{0.95}\text{Ce}_{0.05}\text{FeO}_3$ compared with BiFeO_3 . The latter sometimes displays strange discharge profiles.

3.5. In Situ XRD during Galvanostatic Cycling. It was found in the battery's dissembling process that LiBi alloy formed is very reactive and very easily to be oxidized as soon as it was exposed to ambient environment. Thus, *in situ* measurements of the electronic as well as structural changes are very essential.

To investigate the structural changes of $\text{Bi}_{0.95}\text{Ce}_{0.05}\text{FeO}_3$, *in situ* XRD patterns were recorded during the cycling process and are displayed in Figures 7a and 7b. During the first discharge, the intensity of BiFeO_3 diffraction peaks decreased, while no new diffraction peaks were observed. Also, during the discharge process, there are shifts of diffraction peaks, which indicate that the discharge process is a lithium insertion process and is similar to that of the pure BiFeO_3 .¹⁷ This is different from the discharge mechanisms of other binary transition metal oxides and FeBO_3 , where the active materials decomposed gradually to nano metallic particles embedded in Li_2O matrix in the first discharge.^{5,6,26,34} *In situ* XRD patterns during the first charge process are displayed in Figure 7b. At the fully charged state, diffraction features of BiFeO_3 phase can still be fully observed, indicating that the perovskite matrix is well maintained even after fully separation of Bi ions. Fe ions are responsible to maintain the structural stability. During discharge, shifts of perovskite diffraction peaks are also observed, indicating that Li ions are extracted out of the lattice. However, the intensity of the diffraction peaks are not affected by Li ions extraction, indicating that the perovskite matrix is well maintained after lithium extraction.

The difference diffraction patterns (subtract the diffraction pattern at the end of the first discharge) are displayed in Figure 7c. In the first charge process, the diffraction peaks of Bi can be barely observed (the standard diffraction pattern of metallic Bi are displayed in the bottom in black), indicating that the particle size of the metallic Bi is very small. However, during the

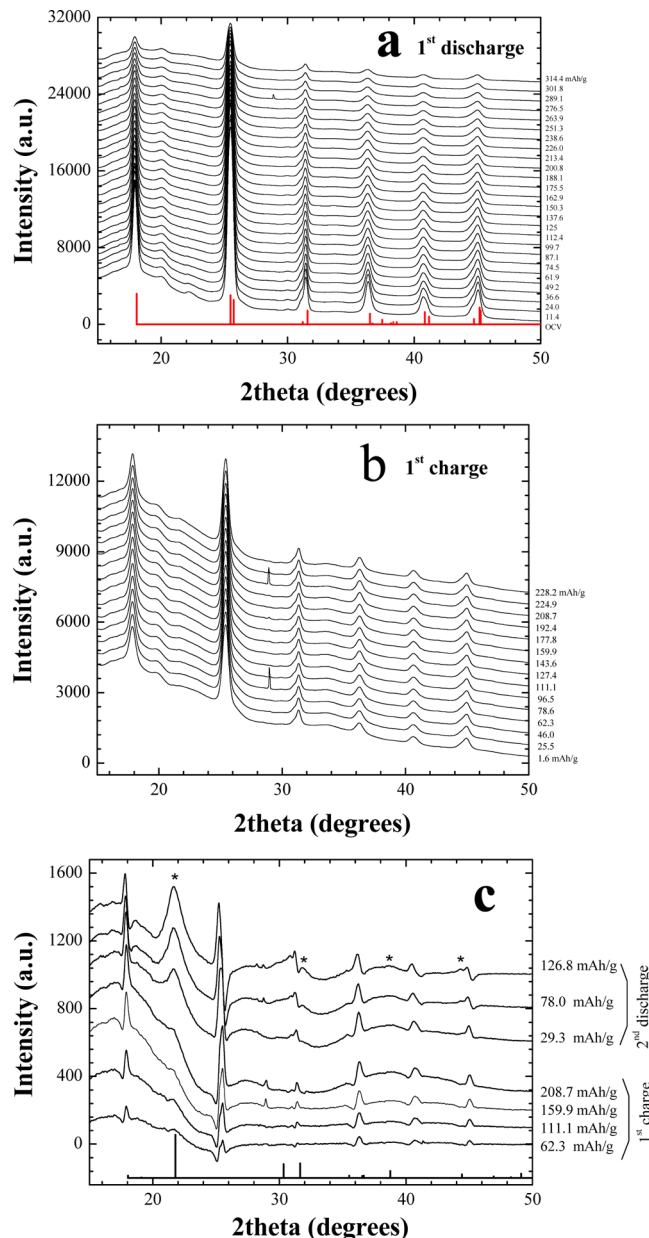


Figure 7. (a) *In situ* XRD patterns collected during the first discharge of $\text{Bi}_{0.95}\text{Ce}_{0.05}\text{FeO}_3$ -Li battery using the spectroelectrochemical cell feature. The diffraction pattern of standard BiFeO_3 was displayed at the bottom (red). (b) *In situ* XRD patterns collected during the first charge of $\text{Bi}_{0.95}\text{Ce}_{0.05}\text{FeO}_3$ -Li battery using the spectroelectrochemical cell feature. (c) Difference diffraction patterns collected at different stage of first charge and second discharge. The XRD patterns displayed have subtracted the diffraction pattern of the one at the end of first discharge cycle.

second discharge, the metallic Bi diffraction peaks vastly increased, and the other diffraction features (marked by asterisks) can also be clearly identified. This indicates a fast increase of particle size of metallic Bi during the second discharge.

The *in situ* diffraction patterns were fitted using the EXPGUI code, and the lattice parameters are displayed in Figures 8a and 8b for *c*- and *a/b*-axis, respectively. During the first discharge, the *c*-axis continuously increased until ~150 mAh/g, and after that, it started to decrease. The capacity of 150 mAh/g is consistent with two-electron transfer and indicates the

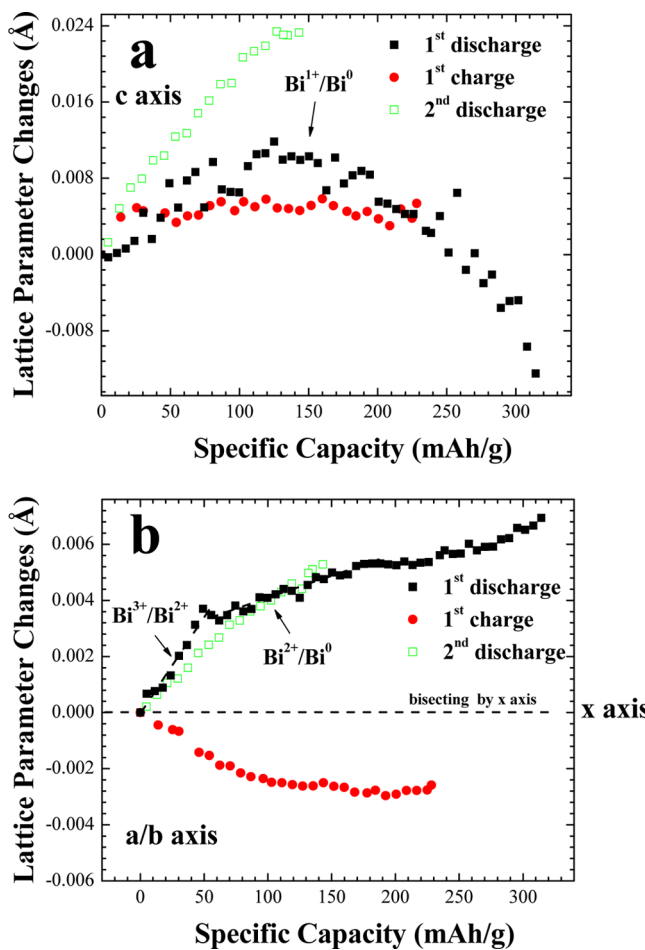


Figure 8. (a) Detailed analysis of lattice parameter changes of $\text{Bi}_{0.95}\text{Ce}_{0.05}\text{FeO}_3$ (c -axis) in the electrochemical cycling process: black, first discharge; red, first charge; green, second discharge. (b) Detailed analysis of lattice parameter changes (a/b -axis) in the electrochemical cycling process: black, first discharge; red, first charge; green, second discharge. In the second discharge, the battery was stopped at ~ 140 mAh/g due to beamtime cutoff.

reduction of Bi^{3+} to Bi^{1+} . The increase of c lattice parameter is the result of lithium insertion. After 150 mAh/g, the Bi^{1+} ions are further reduced to metallic Bi, which induced a large c -axis lattice parameters decrease. This indicates that metallic Bi came out of heavily lithiated BiFeO_3 lattice and contributed to a vast shrinkage of the c -lattice. This is similar to the effect of Bi^{3+} substitution by Ce^{3+} , which decreased the c -axis lattice parameters as well. The *in situ* XRD patterns observed here is different from those observed during the discharge of FeBO_3 , where the active materials transformed into amorphous in the first discharge process.^{26,47,48} At the fully discharge stage, the diffraction peaks of BiFeO_3 can still be clearly observed even after fully separation of Bi ions.

During first discharge, the a/b -axis increased gradually, consisted with Li^+ insertion into the perovskite matrix. Fast increase of the a/b -axis is observed before ~ 50 mAh/g, and after that, the trend of increase is less. The capacity of 50 mAh/g is consistent with the reduction of Bi^{3+} to Bi^{2+} . Between 50 and 160 mAh/g, second slope of the a -axis lattice parameter increase is observed and is consistent with the further reduction of Bi ions. However, compared with the c -axis, a/b -axis did not display a decrease during the discharge, even after fully

separation of Bi ions. This indicates that the a/b -axis is mainly expanded by Li ions insertion.

During first charge, the a/b -axis displayed large decrease before 100 mAh/g, and after that, they slightly decreased until the fully charged state. The a -axis lattice parameter changes in the first charge cycle is like a mirror image of that in the first discharge, bisecting by the x -axis. Since after fully discharge, there are no Bi ions in the perovskite matrix, and thus, the change of the a/b -axis is mainly affected by Li ions insertion. However, the c -axis displays an increase at a capacity of 10 mAh/g and stays almost constant after that. This is in a different trend compared with that of the a/b -axis. In the second discharge, the a/b -axis increases gradually as the insertion of Li ions and is more like a mirror image of that during the first charge process.

Overall, the a/b -axis's lattice parameter change during both the charge and discharge process are mainly dominated by Li ions intercalation/deintercalation. However, the species in the c -axis has a larger effect on the c -axis lattice parameter change. Since Li ions intercalation/deintercalation is typical for ionic conduction, and Bi ions reduction is an electronic transfer process, thus, this indicated that $\text{Bi}_{0.95}\text{Ce}_{0.05}\text{FeO}_3$ has two distinct conduction pathways. One is the ionic conduction pathway, and the other is the electronic conduction pathway, which is along the c -axis direction.

3.6. *In Situ* Bi L_{III}-Edge XANES during Galvanostatic Cycling.

The *in situ* Bi L_{III}-edge XANES spectra of $\text{Bi}_{0.95}\text{Ce}_{0.05}\text{FeO}_3$ –Li battery during the first charge are displayed in Figure 9. Two features are mainly observed. First, the Bi L_{III}-

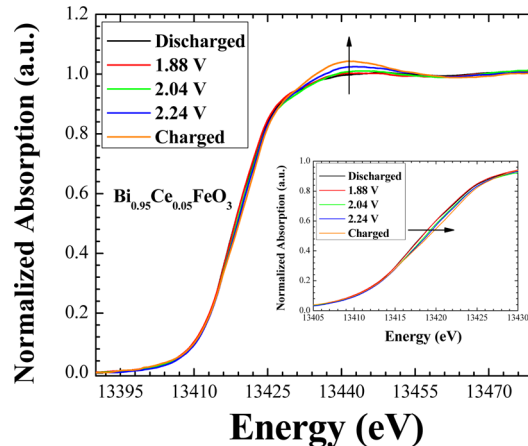


Figure 9. *In situ* Bi L_{III}-edge XANES spectra collected during the charge process of $\text{Bi}_{0.95}\text{Ce}_{0.05}\text{FeO}_3$ –Li battery using the spectroelectrochemical cell feature: black, at the end of first discharge; red, charged to 1.88 V; green, charged to 2.04 V; blue, charged to 2.24 V; orange, at the end of first charge. The voltage window is between 1.15 and 3.0 V. Inset displays enlarged view of the edge shift.

edge is shifted toward higher energy position. Second, the white-line intensity of the Bi L_{III}-edge increased gradually. This indicates that metallic Bi formed in the first discharge process is gradually oxidized back to its ionic state. This also indicates that Bi ions are responsible for charge transfer in the first charging process. However, compared with the Bi L_{III}-edge spectra during the discharge process,¹⁷ those during the charge process displayed much less shift. This indicates that Bi is not fully oxidized back to their +3 oxidation state during the

electrochemical charge process and contributes to the capacity loss in the following discharges.

The discharge mechanisms observed in $\text{Bi}_{0.95}\text{Ce}_{0.05}\text{FeO}_3$ is different from what has been observed in some other perovskite-type oxides, such as FeBO_3 ,²⁶ $(\text{Li},\text{La})\text{TiO}_3$,²⁵ and $\text{Gd}_{1/3}\text{TaO}_3$ ²¹ etc., where the B site ions are mainly responsible for charge transfer. However, in the case of $\text{Bi}_{0.95}\text{Ce}_{0.05}\text{FeO}_3$, A site ions are mainly responsible for charge transfer and Fe ions are mainly responsible to maintain the structural integrity of the ceramic matrix. In perovskite oxide-based catalysts, the reactivity of B site cations is normally much more reactive compared with that of A site cations,^{49–51} and this is consistent with the discharge observed for FeBO_3 ,²⁶ $\text{La}_{1/3}\text{NbO}_3$,²⁵ and $\text{Gd}_{1/3}\text{TaO}_3$.²¹ Thus, $\text{Bi}_{0.95}\text{Ce}_{0.05}\text{FeO}_3$ displayed unusual cycling mechanism compared with the previous observation.

4. FURTHER THOUGHTS

1. The a/b lattice parameters change of $\text{Bi}_{0.95}\text{Ce}_{0.05}\text{FeO}_3$ during the cycling process are displayed in Figure 10b. For comparison, the corresponding electrochemical cycling profiles are displayed in Figure 10a. (Since the a/b lattice parameters changes are in the reverse direction compared with the voltage

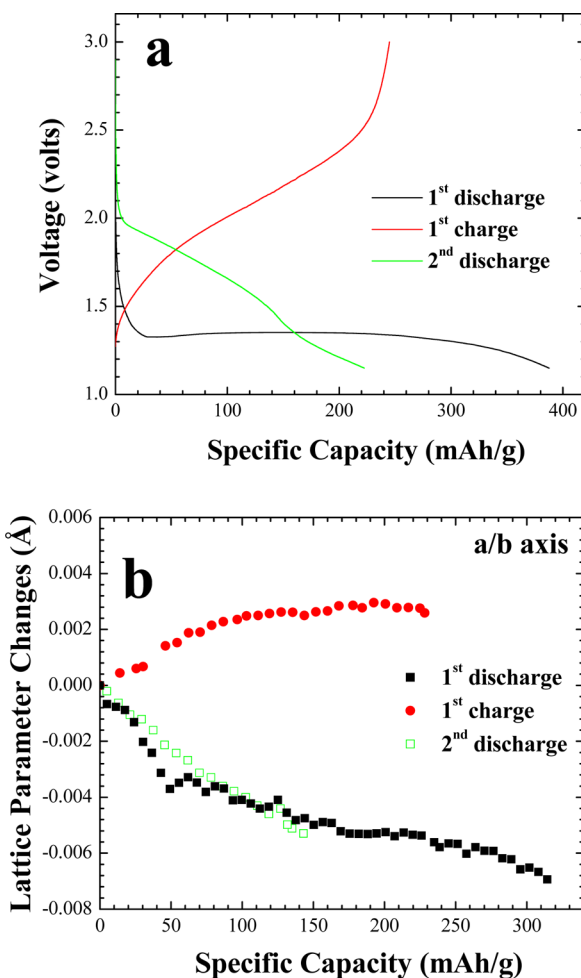


Figure 10. (a) Electrochemical cycling profiles of $\text{Bi}_{0.95}\text{Ce}_{0.05}\text{FeO}_3$ during the first discharge (black), first charge (red), and second discharge (green). (b) Detailed analysis of lattice parameter changes (a/b -axis) during the first discharge (black), first charge (red), and second discharge (green). The a/b -axis lattice parameters changes are multiplied by -1 .

change in the cycling process, they are multiplied by -1 for better comparison.) The lattice parameter change of the a/b -axis is very similar to the electrochemical cycling profile, even after Bi ions separation out of the crystal lattice in the first discharge process. This indicates that Li ions insertion/extraction is not affected by Bi ions. Since the a/b -axis lattice parameter is not affected by Bi ions and that of the c -axis is heavily affected, it is expected that Li ions insertion/extraction happened along the a/b -plane, which is perpendicular to the c -axis direction, and is less affected by the species in the c -axis direction. Thus, the two distinct conduction pathway of $\text{Bi}_{0.95}\text{Ce}_{0.05}\text{FeO}_3$ are along the a/b -plane and c -axis for ionic conduction and electronic conduction, respectively.

2. BiFeO_3 is well-known to exhibit multiferroic properties^{52–55} at ambient temperature and can be ferroelectric and ferromagnetic simultaneously. The lone electron pair of Bi ions is responsible for the ferroelectric property, and Fe ions are responsible for the magnetism. As reported in the literature, the ferroelectric polarization direction of BiFeO_3 is along the diagonal of rhombohedral lattice, which is the c -axis direction if using a hexagonal setting.^{54,55} The magnetic propagation direction of BiFeO_3 is along the 111 plane of the rhombohedral lattice, which is the 003 plane of the hexagonal lattice. Thus, the electric polarization direction is the same as the electronic conduction direction, and the magnetic propagation direction is the ionic conduction direction, which is along the a/b -plane of the hexagonal cell. The lattice parameter changes observed during the electrochemical cycling of $\text{Bi}_{0.95}\text{Ce}_{0.05}\text{FeO}_3$ –Li battery give a clear structural correlation with its multiferroic property.

5. SUMMARY

BiFeO_3 and $\text{Bi}_{0.95}\text{Ce}_{0.05}\text{FeO}_3$ were synthesized via a coprecipitation technique. During the synthesis process, the phase transitions were monitored via *in situ* synchrotron XRD. During the synthesis process, there are intermediate phases appeared, such as $\text{Bi}_{24}\text{Fe}_2\text{O}_{39}$ and $\text{Bi}_{25}\text{FeO}_{40}$. The Ce addition increased the formation temperature of BiFeO_3 , while greatly suppressed the particle size growth, which facilitates the electrochemical discharge. Ce doping decreases both the c - and a -axis lattice parameters. $\text{Ce}_{0.05}\text{Bi}_{0.95}\text{FeO}_3$ was further used for lithium battery application. Compared with BiFeO_3 synthesized using the similar technique, Ce doping not only increased the discharge capacity (with a cutoff voltage of 1.15 V) but also displayed 0.15 V higher discharge voltage after the first cycle. The lattice parameters of $\text{Bi}_{0.95}\text{Ce}_{0.05}\text{FeO}_3$ were monitored using synchrotron-based *in situ* XRD. After 2 lithium ions insertion, Bi ions are reduced to metallic state and separated out of the perovskite lattice. In the following charge process, metallic Bi can be oxidized back to its ionic state. Elevated voltage discharges were observed in the following cycles. There are two distinct conduction pathways: One is the ionic conduction pathway along the a/b -plane, and the other is the electronic conduction pathway along the c -axis. The ionic conduction is critical for the shape of electrochemical cycling while the electronic conduction is critical for the voltage of the discharge. The lattice parameters change during the electrochemical cycling process of $\text{Bi}_{0.95}\text{Ce}_{0.05}\text{FeO}_3$ –Li battery give a direct correlation with the structure and the multiferroic property.

■ ASSOCIATED CONTENT

Supporting Information

Full information on refs 7 and 52. This material is available free of charge via the Internet at <http://pubs.acs.org>.

■ AUTHOR INFORMATION

Corresponding Author

*E-mail: wenwen@sinap.ac.cn.

Notes

The authors declare no competing financial interest.

■ ACKNOWLEDGMENTS

The work was supported by the National Basic Research Program of China (973 Program) (Grants 2010CB934501 and 2010CB934503), National Natural Science Foundation of China (NSFC) (Grants 10979073 and 21203235), Science and Technology Commission of Shanghai Municipality (Grant 1052nm07800), and Institutional Innovation grant (Grant O95501E061) of the Shanghai Institute of Applied Physics, CAS. The authors also thank beamlines BL14B1 and BL14W1 of SSRF (Shanghai Synchrotron Radiation Facility) for providing the beam time. The valuable discussions with Dr. Jonathan C. Hanson were highly appreciated.

■ REFERENCES

- (1) Ceder, G.; Chiang, Y.-M.; Sadoway, D. R.; Aydinol, M. K.; Jang, Y.-I.; Huang, B. *Nature* **1998**, *392*, 694–696.
- (2) Tsai, Y. W.; Hwang, B. J.; Ceder, G.; Sheu, H. S.; Liu, D. G.; Lee, J. F. *Chem. Mater.* **2005**, *17*, 3191–3199.
- (3) Uchimoto, Y.; Sawada, H. *J. Power Sources* **2001**, *97*, 326–327.
- (4) Shin, Y.; Manthiram, A. *Electrochim. Acta* **2003**, *48*, 3583–3592.
- (5) Gruegeon, S.; Laruelle, S.; Dupont, L.; Tarascon, J.-M. *Solid State Sci.* **2003**, *5*, 895–904.
- (6) Poizot, P.; Laruelle, S.; Gruegeon, S.; Dupont, L.; Tarascon, J.-M. *Nature* **2000**, *407*, 496–499.
- (7) Wang, F.; Robert, R.; Chernova, N. A.; Pereira, N.; Omenya, F.; Badway, F.; Hua, X.; Ruotolo, M.; Zhang, R. G.; Wu, L. J.; et al. *J. Am. Chem. Soc.* **2011**, *133*, 18828–18836.
- (8) Dambournet, D.; Chapman, K. W.; Chupas, P. J.; Gerald, R. E., II; Penin, N.; Labrugere, C.; Demourgues, A.; Tressaud, A.; Amine, K. *J. Am. Chem. Soc.* **2011**, *133*, 13240–13243.
- (9) Wang, X. L.; Han, W. Q.; Chen, H. Y.; Bai, J. M.; Tyson, T. A.; Yu, X. Q.; Wang, X. J.; Yang, X. Q. *J. Am. Chem. Soc.* **2011**, *133*, 20692–20695.
- (10) Lacorre, P.; Goutenoire, F.; Bohnke, O.; Retoux, R.; Laligant, Y. *Nature* **2000**, *404*, 856–858.
- (11) Stevenson, J. W.; Armstrong, T. R.; Carneim, R. D.; Pederson, L. R.; Weber, W. J. *J. Electrochem. Soc.* **1996**, *143*, 2722–2729.
- (12) de Fontaine, D.; Ceder, G.; Asta, M. *Nature* **1990**, *343*, 544–546.
- (13) Teraoka, Y.; Nobunaga, T.; Okamoto, K.; Miura, N.; Yamazoe, N. *Solid State Ionics* **1991**, *48*, 207–212.
- (14) Lybye, D.; Poulsen, F. W.; Mogensen, M. *Solid State Ionics* **2000**, *128*, 91–103.
- (15) Orera, A.; Slater, P. R. *Chem. Mater.* **2010**, *22*, 675–690.
- (16) Sharma, N.; Shaju, K. M.; Rao, G. V. S.; Chowdari, B. V. R. *Electrochim. Commun.* **2002**, *4*, 947–952.
- (17) Luo, S. H.; Gao, M.; Chen, J.; Xing, X. R.; Li, Z.; Zhou, X. T.; Wen, W. *J. New Mater. Electrochim. Syst.* **2011**, *14*, 141–146.
- (18) Xia, H.; Yan, F.; Lai, M. O.; Lu, L.; Song, W. D. *Funct. Mater. Lett.* **2009**, *2*, 163–167.
- (19) Li, J.; Dahn, H. M.; Sanderson, R. J.; Todd, A. D. W.; Dahn, J. R. *J. Electrochim. Soc.* **2008**, *155*, A975–A981.
- (20) Sharma, Y.; Sharma, N.; Rao, G. V. S.; Chowdari, B. V. R. *Chem. Mater.* **2008**, *20*, 6829–6839.
- (21) Imaki, K.; Nakayama, M.; Uchimoto, Y.; Wakihara, M. *Solid State Ionics* **2004**, *172*, 73–76.
- (22) Nakayama, M.; Imaki, K.; Ikuta, H.; Uchimoto, Y.; Wakihara, M. *J. Phys. Chem. B* **2002**, *106*, 6437–6441.
- (23) Shan, Y. J.; Chen, L. Q.; Inaguma, Y.; Itoh, M.; Nakamura, T. *J. Power Sources* **1995**, *54*, 397–402.
- (24) Zhang, D. W.; Xie, S.; Chen, C. H. *J. Electroceram.* **2005**, *15*, 109–117.
- (25) Nakayama, M.; Usui, T.; Uchimoto, Y.; Wakihara, M.; Yamamoto, M. *J. Phys. Chem. B* **2005**, *109*, 4135–4143.
- (26) Ibarra-Palos, A.; Darie, C.; Proux, O.; Hazemann, J. L.; Aldon, L.; Jumas, J. C.; Morcrette, M.; Strobel, P. *Chem. Mater.* **2002**, *14*, 1166–1173.
- (27) Rodriguez, J. A.; Hanson, J. C.; Frenkel, A. I.; Kim, J. Y.; Perez, M. *J. Am. Chem. Soc.* **2002**, *124*, 346–354.
- (28) Chupas, P. J.; Ciraolo, M. F.; Hanson, J. C.; Grey, C. P. *J. Am. Chem. Soc.* **2001**, *123*, 1694–1702.
- (29) Kim, J. Y.; Rodriguez, J. A.; Hanson, J. C.; Frenkel, A. I.; Lee, P. *L. J. Am. Chem. Soc.* **2003**, *125*, 10684–10692.
- (30) Toby, B. H. *J. Appl. Crystallogr.* **2005**, *38*, 1040–1041.
- (31) Yoon, W. S.; Balasubramanian, M.; Chung, K. Y.; Yang, X. Q.; McBreen, J.; Grey, C. P.; Fischer, D. A. *J. Am. Chem. Soc.* **2005**, *127*, 17479–17487.
- (32) Ein-Eli, Y.; Lu, S. H.; Rzeznik, M. A.; Mukerjee, S.; Yang, X. Q.; McBreen, J. *J. Electrochem. Soc.* **1998**, *145*, 3383–3386.
- (33) Lv, D. P.; Wen, W.; Huang, X. K.; Bai, J. Y.; Mi, J. X.; Wu, S. Q.; Yang, Y. *J. Mater. Chem.* **2011**, *21*, 9506–9512.
- (34) Zhong, K. F.; Zhang, B.; Luo, S. H.; Wen, W.; Li, H.; Huang, X. J.; Chen, L. Q. *J. Power Sources* **2011**, *196*, 6802–6808.
- (35) Ravel, B.; Newville, M. *J. Synchrotron Radiat.* **2005**, *12*, 537–541.
- (36) Larson, A. C.; Von Dreele, R. B. GSAS General Structure Analysis System. Report LAUR 86-748, Los Alamos National Laboratory, Los Alamos, NM, 1995.
- (37) Rietveld, H. M. *J. Appl. Crystallogr.* **1969**, *2*, 65–71.
- (38) Toby, B. H. *J. Appl. Crystallogr.* **2001**, *34*, 210–213.
- (39) Reyes, A.; de la Vega, C.; Fuentes, M. E.; Fuentes, L. *J. Eur. Ceram. Soc.* **2007**, *27*, 3709–3711.
- (40) PDF card # 420201.
- (41) PDF card # 460416.
- (42) PDF card # 200836.
- (43) Brinkman, K.; Iijima, T.; Nishida, K.; Katoda, T.; Funakubo, H. *Ferroelectrics* **2007**, *357*, 35–40.
- (44) Quan, Z. C.; Hu, H.; Xu, S.; Liu, W.; Fang, G. J.; Li, M. Y.; Zhao, X. Z. *J. Sol-Gel Sci. Technol.* **2008**, *48*, 261–266.
- (45) Chen, J.; Xing, X. R.; Watson, A.; Wang, W.; Yu, R. B.; Deng, J. X.; Yan, L.; Sun, C.; Chen, X. B. *Chem. Mater.* **2007**, *19*, 3598–3600.
- (46) Gmitter, A. J.; Badway, F.; Rangan, S.; Bartynski, R. A.; Halajko, A.; Pereira, N.; Amatucci, G. G. *J. Mater. Chem.* **2010**, *20*, 4149–4161.
- (47) Rowsell, J. L. C.; Gaubicher, J.; Nazar, L. F. *J. Power Sources* **2001**, *97*–8, 254–257.
- (48) Palos, A. I.; Morcrette, M.; Strobel, P. *J. Solid State Electrochem.* **2002**, *6*, 134–138.
- (49) Goodenough, J. B. *Rep. Prog. Phys.* **2004**, *67*, 1915–1993.
- (50) Tilset, B. G.; Fjellvag, H.; Kjekshus, A. *J. Solid State Chem.* **1995**, *119*, 271–280.
- (51) Buciuman, F. C.; Patcas, F.; Menezo, J. C.; Barbier, J.; Hahn, T.; Hans-Günther Lintz, H. G. *Appl. Catal. B: Environ.* **2002**, *35*, 175–183.
- (52) Wang, J.; Neaton, J. B.; Zheng, H.; Nagarajan, V.; Ogale, S. B.; Liu, B.; Viehland, D.; Vaithyanathan, V.; Schlom, D. G.; Waghmare, U. V.; et al. *Science* **2003**, *299*, 1719–1722.
- (53) Catalan, G.; Scott, J. F. *Adv. Mater.* **2009**, *21*, 2463–2485.
- (54) Chu, Y. H.; Martin, L. W.; Holcomb, M. B.; Ramesh, R. *Mater. Today* **2007**, *10*, 17–23.
- (55) Ederer, C.; Spaldin, N. A. *Phys. Rev. B* **2005**, *71*, 060401.